Article:
Shi, W, Mills, BJW orcid.org/0000-0002-9141-0931, Li, C et al. (6 more authors) (2022) Decoupled oxygenation of the Ediacaran ocean and atmosphere during the rise of early animals. Earth and Planetary Science Letters, 591. 117619. ISSN 0012-821X

https://doi.org/10.1016/j.epsl.2022.117619

Decoupled oxygenation of the Ediacaran ocean and atmosphere during the rise of early animals

Wei Shi[a], Benjamin J. W. Mills[b], Chao Li[a,c]*, Simon W. Poulton[b,d], Alexander J. Krause[b,e], Tianchen He[b], Ying Zhou[e], Meng Cheng[c], Graham A. Shields[e]

[a] *State Key Laboratory of Biogeology and Environment Geology, China University of Geosciences, Wuhan, China.*

[b] *School of Earth and Environment, University of Leeds, Leeds, LS2 9JT, UK*

[c] *State Key Laboratory of Oil and Gas Reservoir Geology and Exploitation & Institute of Sedimentary Geology, Chengdu University of Technology, Chengdu 610059, China*

[d] *State Key Laboratory of Geological Processes and Mineral Resources, China University of Geosciences, Wuhan, China.*

[e] *Department of Earth Sciences, University College London, London WC1E 6BT, UK*

**E-mail address: chaoli@cug.edu.cn or chaoli@cdut.edu.cn*

Abstract

The Ediacaran Period (~635 to 541 Ma) witnessed the early diversification and radiation of metazoans, in the form of the Ediacaran Biota. This biological revolution, beginning at ~575 Ma, has been widely attributed to a temporally restricted episode of deeper ocean oxygenation, potentially caused by a contemporaneous rise in atmospheric oxygen levels. However, quantitative geochemical-record-driven estimates of Ediacaran atmospheric and oceanic redox evolution are lacking, and hence possible links between oceanic and atmospheric oxygenation remain speculative. Here, after screening for possible post-depositional alteration, we utilize paleogeographically-diverse carbon and sulfur isotope records from South China, Oman and USA-Mexico, to develop a biogeochemical isotope mass balance model to quantify Ediacaran atmospheric oxygen and oceanic sulfate evolution. Model results from all three continents indicate that Ediacaran atmospheric oxygen levels rose monotonically between ~630 Ma and ~590 Ma, and subsequently remained relatively stable at around 0.6 present atmospheric level

for the remainder of the Ediacaran. By contrast, the marine sulfate reservoir appears to have remained relatively stable before ~575 Ma, with a subsequent large pulse where sulfate concentrations rose to ~8 mM. These quantitative results indicate that Ediacaran oceanic and atmospheric oxygenation were decoupled, which is consistent with published geochemical records. We propose that the early Ediacaran rise of atmospheric oxygen levels, driven by increased net burial of organic carbon and pyrite, may not have established widespread deep-ocean oxygenation. Instead, later pulsed input of oxidizing power (mainly sulfate) from the continents drove transient episodes of seafloor oxygenation that accompanied radiations of the Ediacaran Biota.

Highlights

- Systematic quantification of Ediacaran atmospheric oxygen levels and oceanic sulfate concentrations
- An isotope mass balance technique forced by global C-S isotopic records
- Decoupled atmospheric and oceanic oxygenation
- Marine oxygenation lagged behind atmospheric O_2 rise

Key words: Ediacaran, atmospheric oxygen, oceanic sulfate, isotope mass balance, Metazoan evolution

1. Introduction

Molecular oxygen (O_2) is a critical factor in terms of Earth's habitability for complex life forms, and its accumulation proceeded in broad steps (Lyons et al., 2014) (Fig. 1a). The Great Oxidation Event (GOE) from ~2.43 to 2.22 Ga (Poulton et al., 2021) witnessed the first major rise in atmospheric O_2 (pO_2), from $<10^{-6}$ times the present atmospheric level (PAL) prior to the GOE, to values that are widely debated, but are generally estimated to be between ~10^{-3}-10^{-1} PAL during the mid-Proterozoic (Daines et al., 2017). The second major oxidation of Earth's surficial environment occurred during the Neoproterozoic Oxygenation Event (NOE) (Och and Shields, 2012). This rise in atmospheric O_2 between ~800 Ma and ~550 Ma has a theoretical upper limit of ~0.5-0.7 PAL when considering possible nutrient levels in Precambrian anoxic oceans (Lenton et al., 2014) (Fig. 1b). These upper

limits are inferred from the amount of oxygen theoretically required to oxygenate the 'deep ocean' (i.e., subsurface waters ranging from continental shelves to abyssal plains), and are in line with the sporadic appearance of sediments deposited under oxic deep-water conditions during the late Neoproterozoic (e.g., Canfield et al., 2007; Pogge Von Strandmann et al., 2015; Sahoo et al., 2016; Zhang et al., 2019). This potential coupling between atmospheric and oceanic oxygenation (note that, in this study, "oceanic oxygenation" is indicated by the significant increase of marine sulfate concentration) has widely been interpreted as a trigger for the rapid evolution of morphologically complex multicellular eukaryotes (e.g., Canfield et al., 2007; Lyons et al., 2014; Brocks et al., 2017), culminating in metazoan diversification and radiation in the form of the Ediacaran Biota (Darroch et al., 2018).

Compilations of the oceanic inventories of redox sensitive elements (e.g., Mo, V and Re) (e.g., Sahoo et al., 2016) and iron-speciation (e.g., Canfield et al., 2008; Sperling et al., 2015a; Sahoo et al., 2016) document widespread euxinic (anoxic, containing free H_2S) and ferruginous conditions (anoxic, containing free Fe^{2+}) in Ediacaran mid-depth and deep waters (Li et al., 2010), with a temporally restricted episode of deeper ocean oxygenation, especially after the Gaskiers glaciation at ~575 Ma (Fig. 1c). This dominance of anoxic deeper waters throughout much of the Ediacaran implies that atmospheric O_2 generally remained low (Li et al., 2020), but with potential variability, although marine redox state does not in itself accurately map atmospheric O_2 evolution.

Another proxy for ocean oxygenation is the inventory of oceanic sulfate ($[SO_4^{2-}]_{sw}$), and its reconstruction offers an opportunity to assess oxidant levels in the Ediacaran ocean (Fig. 1d). Some reconstructions yield a lower $[SO_4^{2-}]_{sw}$ estimate of <2 mM from the early Ediacaran onwards (e.g., Loyd et al., 2012; Osburn et al., 2015), with a significant increase to >8 mM on the marine shelf (e.g., Shi et al., 2018) during the mid-Ediacaran Shuram Excursion (SE; also known as EN3 [McFadden et al., 2008] or DOUNCE in South China [Lu et al., 2013], representing the largest known negative carbonate C-isotope [$\delta^{13}C_{carb}$] excursion in Earth history [Grotzinger et al., 2011]). However, there are also estimates for both higher Ediacaran $[SO_4^{2-}]_{sw}$ of >17 mM, as inferred from multiple sulfur isotope data and fluid inclusions in halite (e.g., Brennan et al., 2004), and lower $[SO_4^{2-}]_{sw}$ of <0.03 mM, based on the occurrence of 'super-heavy' pyrite isotope signatures (e.g., Tostevin et al., 2017). A $[SO_4^{2-}]_{sw}$ range of 6–10 mM has also been estimated during the latest Ediacaran, based on calcium isotope ratios of bedded sulfate evaporites (Blättler et al., 2020) (Fig. 1d). These highly uncertain and

contradictory estimates for $[SO_4^{2-}]_{sw}$, which are based on relatively sparse data, mean that Ediacaran oceanic sulfate levels are poorly known. As such, it is unclear whether Ediacaran marine oxygenation events were driven by large pulses of atmospheric O_2 against a backdrop of very low sulfate levels, or whether a long-term rise in atmospheric O_2 poised the system at a level that was close to the threshold for widespread marine oxygenation. These uncertainties are critical to resolve in order to understand the global processes and mechanisms responsible for Ediacaran ocean oxygenation and its biological effects.

Ediacaran atmospheric and oceanic redox evolution can be quantitatively estimated by biogeochemical models which consider most major biogeochemical principles and factors. A recent estimate of rising pO_2 and $[SO_4^{2-}]_{sw}$ over the Ediacaran was made using a forwards modelling approach, whereby these changes were driven by an increasing length of subduction zones, in which increased rates of tectonic CO_2 degassing resulted in higher nutrient delivery from continental weathering, and hence higher burial rates of organic carbon (Williams et al., 2019) (Fig. 1e). Whilst insightful, this model predicts static C- and S-isotope sedimentary records that contrast with observed geological variability (Williams et al., 2019). There is thus a clear requirement for geochemical-record-driven modeling estimates of Ediacaran atmospheric and oceanic redox evolution.

In this study, we apply an Isotope Mass Balance (IMB) approach to quantitatively estimate the evolution of Ediacaran atmospheric and oceanic oxygenation (Mills et al., 2016). This technique uses measured geological C- and S-isotope records to reconstruct the long-term organic carbon and pyrite burial fluxes, which are the principal sources of O_2 over geological timescales, and has been successfully employed within the GEOCARBSULF model for Phanerozoic O_2 estimation. We embed the IMB technique within the COPSE model (Mills et al., 2016), which has the advantage of using an implicit variable-order integration method (Lenton et al., 2018) that greatly reduces model failure rate and allows testing of more extreme scenarios (Mills et al., 2016). We further compiled a large dataset (1418 data points) of published paired $\delta^{13}C_{carb}$ and carbonate-associated sulfate-sulfur isotope data ($\delta^{34}S_{CAS}$), with $\Delta^{34}S$ measurements (the difference between $\delta^{34}S_{CAS}$ and coexisting pyrite sulfur isotope values [$\delta^{34}S_{py}$]) from three typical Ediacaran continental margin successions (Oman, South China and USA-Mexico; Figs. 1f and 2; see below and Supplementary Information for details of study regions and data sources). While each site in isolation may represent a local shelf signal, continental shelves were the major loci for global primary productivity and pyrite burial, and thus our

combined data can be considered more generally to reflect broad global trends. As such, we use these data to drive our IMB-COPSE model, in order to quantitatively estimate Ediacaran atmospheric and oceanic redox evolution.

2. Material and method

2.1 Study regions, data compilation and screening

The studied Ediacaran strata are well-preserved and a global correlation of these strata can be made using a variety of techniques, including stratigraphy, paleobiology and geochronology (Fig. 1f; Grotzinger et al., 2011). The three study regions were located on different plates during the Ediacaran (Fig. S1), comprising the Afif-Abas Terrane (Oman), South China Plate (South China) and Northwestern Laurentia (USA-Mexico). All of the study regions are thought to have been generally connected with the open ocean throughout the Ediacaran and early Cambrian (Fig. S1). The three study regions were chosen not only because they were located on different continents, and thus are of global significance, but also because $\delta^{13}C_{carb}$ and paired $\delta^{34}S_{CAS}$-$\delta^{34}S_{py}$ records have been successfully reported for these regions, thus offering a complete data source for our IMB-COPSE model (Fig. 2). The studied strata in Oman consists of the Nafun Group from MQR-1 and TM-6 drill cores, and the integrated dataset is a compilation of all Ara South Oman Salt Basin data; the South China dataset includes data from three sections: the Jiulongwan section (Hubei Province), the Gaojiashan section (Shannxi Province) and the Lianghekou section (Shannxi Province); the USA-Mexico dataset is a combination of data from two major sections located in Death Valley, California, western USA, and in Cerro Rajón, Sonora, northern Mexico.

Obtaining carbon-sulfur isotopic signals of primary seawater provides the foundation for IMB model results (Mills et al., 2016). Literature data were screened for possible post-depositional alteration, whereby: (i) we exclude data from samples with Mn/Sr > 10 or $\delta^{18}O_{carb} < -10‰$, which likely reflect significant diagenetic-fluid alteration (Kaufman and Knoll, 1995); (ii) we examined $\delta^{34}S$ values relative to the concentration of carbonate-associated sulfate ([CAS]), and excluded data from samples with both anomalously high [CAS] (>10000 ppm) and extremely low $\delta^{34}S_{CAS}$ (<10‰), which are likely caused by post-depositional pyrite oxidation; (iii) we excluded $\delta^{34}S_{py}$ data for samples containing large pyrite crystals, due to the potential for late stage diagenetic or metamorphic alteration; (iv) we averaged repeat data and applied a LOWESS (LOcally WEighted Scatterplot Smoothing)

approach to determine a best-fit trend for the irregularly distributed time-series of $\delta^{13}C$ and $\delta^{34}S$ data (Fig. 2), and further developed sensitivity tests to dampen any outlier effects arising from post-depositional alteration on the overall trends in our modelling results (see Supplementary Information for details); and (v) we excluded all Ediacaran cap carbonate data from our compilation because these carbonates usually show signs of diagenesis or late-stage alteration, as suggested by their Ca- and Mg- isotope compositions (e.g., Ahm et al., 2019) (see Table S8 and Supplementary Information for more details of the C-S dataset). Finally, we develop more sensitivity tests to compare the effects with or without diagenesis screening on the model results. Sensitivity tests show that outliers arising from post-depositional alteration have limited effects on the overall trends in $\delta^{13}C$ and $\delta^{34}S$ thus the final modelled results (see Supplementary Information for more details).

2.2 Stratigraphic correlation and age framework

The stratigraphic basis for the global subdivision and correlation of Ediacaran strata remains controversial due to the dearth of skeletal fossils, uncertainties in sequence boundaries, and unconformities in many sections (Xiao et al., 2016). However, climatic and chemostratigraphic events (e.g., the Gaskiers glaciation and SE) can potentially be used to correlate Ediacaran strata (Rooney et al., 2020). Six age frameworks have been suggested for correlations of the Ediacaran System, which are based on independent calibrations using available radiometric dates and biostratigraphic data, yet, the onset and termination of the SE event are still debated (e.g., Xiao et al., 2016; Rooney et al., 2020; Yang et al., 2021) (see Tables S1-2 and Supplementary Information for more details). Here, we integrate the carbon-sulfur isotope records of the three study regions based on 'Framework 1' in Table S2, whereby the onset of the SE occurred after ~575 Ma, as indicated by a Re-Os age of 574±4.7 Ma (Rooney et al., 2020), which is coincident with the oldest metazoan fossils. Termination of the SE occurred by ~567 Ma, as constrained by a Re-Os age of 567.3±3.0 Ma (Rooney et al., 2020), and thus the SE lasted ~8 Myr. We use Framework 1 as this represents the only framework where both radioisotopic Re-Os ages and $\delta^{13}C_{carb}$ data are available for the same section (Rooney et al., 2020). In order to explore the individual study region in more detail, we further arranged the dataset using existing radioisotopic ages (Tables S1-2) and published stratigraphic correlations for each region. Since the stratigraphic correlations are still in dispute, we also tested alternative age frameworks, which result in different durations for the SE (i.e., ~15 Myrs, ~25 Myrs, etc.). However, we note that

the specific duration of the SE does not change our conclusions (see Figs. S2, S3 and Supplementary Information for more details).

2.3 Model development and key parameters

Figure 3 shows the fluxes, reservoirs, and their relationships in the IMB-COPSE model (Mills et al., 2016). Oxygen is released via burial (B) of photosynthetically-derived carbon and pyrite sulfur (blue arrows in Fig. 3), and is removed by weathering (W) or metamorphic degassing (D) (red arrows in Fig. 3). The source-sink mass balance for O_2 is:

$$\frac{dO_2}{dt} = B(G) - \mathrm{W}(G_y) - \mathrm{W}(G_a) - \mathrm{D}(G_a) + 2 \times [B(PYR) - \mathrm{W}(PYR_y) - \mathrm{W}(PYR_a) - \mathrm{D}(PYR_a)] \quad (1)$$

where G and PYR are buried organic carbon and pyrite, respectively. Subscripts "y" and "a" denote young and ancient crustal reservoirs, respectively (see below). Due to kinetic selection during photosynthesis and microbial sulfate reduction (MSR), the derived organic carbon and pyrite tend to take up lighter isotopes, which alters the isotopic composition of the marine carbon and sulfur reservoirs (i.e., $\delta^{13}C_{carb}$ and $\delta^{34}S_{CAS}$). Hence, the geological $\delta^{13}C_{carb}$ and $\delta^{34}S_{CAS}$ records can be used to back-calculate the required rate of burial of organic carbon and pyrite sulfur, and therefore the rate of oxygen production. Burial, weathering and degassing of the oxidized forms of carbon and sulfur (black arrows in Fig. 3) impact estimated oxygen concentrations indirectly, by affecting the size and isotopic composition of the surface (e.g., ocean and atmosphere) reservoirs (A: carbon, S: sulfur) and the overall elemental cycling rate (Mill et al., 2016; Lenton et al., 2018). Because the model also calculates weathering and degassing fluxes, the sinks of O_2 are quantified, allowing for a prediction of pO_2 variability in a manner similar to the GEOCARBSULF model for the Phanerozoic. The IMB-COPSE model was used to calculate biogeochemical feedbacks, in which the burial rates of organic carbon and pyrite were back-calculated with the following standard isotope mass balance equations (2) and (3). The model follows the work of Mills et al. (2016), and is solved in MATLAB using the ODE (Ordinary Differential Equation) suite (see https://bjwmills.com for model code). Here, we provide a basic description of the model comprising the key features, and a full description is provided in the Supplementary Information.

The standard IMB equations for the burial fluxes of organic carbon and pyrite sulfur are as

follows:

$$B(G) = \frac{1}{\Delta C}\{[\delta(A) - \delta(G_y)] \times W(G_y) + [\delta(A) - \delta(G_a)] \times [W(G_a) + D(G_a)] + [\delta(A) - \delta(C_y)] \times W(C_y) + [\delta(A) - \delta(C_a)] \times [W(C_a) + D(C_a)]\}. \quad (2)$$

and

$$B(PYR) = \frac{1}{\Delta S}\{[\delta(S) - \delta(PYR_y)] \times W(PYR_y) + [\delta(S) - \delta(PYR_a)] \times [W(PYR_a) + D(PYR_a)] + [\delta(S) - \delta(GYP_y)] \times W(GYP_y) + [\delta(S) - \delta(GYP_a)] \times [W(GYP_a) + D(GYP_a)]\} \quad (3)$$

where $\delta(X)$ is the isotopic composition of reservoir X, and ΔC and ΔS are the isotope fractionations during photosynthesis and microbial sulfate reduction, respectively. Here, ΔS is replaced with observed Δ^{34}S data (Fig. 2), while ΔC is calculated by employing the C-isotope fractionation equation from the original GEOCARBSULF model, rather than using geological data. The reason behind this is that the $\delta^{13}C_{org}$ record during the SE is not co-variant with the $\delta^{13}C_{carb}$ record (e.g., Fike et al., 2006; McFadden et al., 2008; Grotzinger et al., 2011; Li et al., 2017), and may represent exogenetic signals [e.g., dissolved organic carbon (DOC), continental recycled carbon, or petroleum hydrocarbons; see review by Li et al. (2017)] rather than the original photosynthetic-derived organic carbon. Full illustrations of the terms used in Equations (2) and (3) are provided in the Fig. 3 caption.

Following previous work, 'rapid recycling' is included in our IMB-COPSE model in the same way as described in GEOCARBSULF (Mills et al., 2016). This assumes that geologically young sedimentary rocks (with subscript 'y') experience the majority of interaction with the Earth's surface system, including forms of labile carbon and sulfur (e.g., DOC, hydrocarbons, H_2S etc.), but are smaller in size than ancient crustal reservoirs (with subscript 'a'). Mantle reservoirs have not been included in IMB-COPSE, again following the GEOCARBSULF approach (full model details are provided in Supplementary Information with all parameters in Tables S2 to S6).

2.4 Geological background forcings

Attempts to reconstruct atmospheric oxygen evolution must include the fundamental drivers by which the Earth system operates; in particular, the key geological forcings of volcanic degassing (D) and orogenic uplift (U). A compilation of zircon abundance (Voice et al., 2011) (Fig. 4a) combined with globally shorter continental arcs and rifts (Mills et al., 2017) indicates that global rates of

volcanic degassing during the Ediacaran were less than half of the present-day level (PDL) (~40 %; 'D' in Fig. 4e). The global uplift and erosion rates are based on a fit to sediment accumulation rates over time (Hay et al., 2006), where sedimentation rates were reconstructed from sediment masses, thus capturing the overall modulation of uplift by the supercontinent cycle. This is represented in our model with a polynomial fit of $y = 9.5496e^{-0.0031t}$ (Dark purple dashed line in Fig. 4c), which gives an uplift rate of less than 0.2 times the present rate (~0.13-0.19; 'U' in Fig. 4e).

The SE has similar patterns across the globe (Grotzinger et al., 2011), including in South China, Oman, Western USA-Northern Mexico and South Australia, as well as other localities (see summary in Lu et al., 2013), and has been inferred to reflect global-scale oxidation of an organic carbon reservoir (e.g., DOC, recycled continental organic carbon or hydrocarbons; see review by Li et al. (2017)] due to elevated sulfate weathering (e.g., Fike et al., 2006; McFadden et al., 2008; Sawaki et al., 2010; Li et al., 2017; Shields et al., 2019). A previous modelling assessment indicated that in order to sustain the SE for millions of years, an increase of ~7 times the PDL of evaporitic sulfate weathering is required, with the additional sulfate quickly being reduced to pyrite, otherwise the ocean would become rapidly depleted in oxygen (Shields et al., 2019). Palaeomagnetic evidence indicates that the Tonian Period (~1000-720 Ma) witnessed a large evaporite depositional event during the break-up of the Rodinia supercontinent (Evans, 2006). The Ediacaran Period witnessed the convergence of East and West Gondwana (from ~650 to 515 Ma) (Och and Shields, 2012), which may have involved the tectonic inversion of basin-scale evaporite sulfate deposits of Tonian age (Evans, 2006; Shields et al., 2019) (Fig. 4b). These major Tonian evaporite deposits were tectonically exhumed during the middle to late Ediacaran (mostly around ~570 Ma; Shields et al., 2019 and references therein), as supported by an increase in $^{87}Sr/^{86}Sr$ ratios from <0.708 to >0.709 (Sawaki et al., 2010) (Fig. 4a and d) and a decrease in εNd(t) ratios (Wei et al., 2019). Hence, we integrate an additional sulfate weathering pulse of 7 times PDL from 575 to 567 Ma into our IMB-COPSE model ('S_{pulse}' in Fig. 4e), using a similar modelling method to that employed by Shields et al. (2019) (see more details for 'S_{pulse}' in Supplementary Information). Although this theory is supported by widespread evaporite sulfate deposits spanning the Tonian, the timing and magnitude of any pulse in evaporitic sulfate weathering is uncertain, as this process leaves little to no trace in the geological record. Therefore, we also modelled the case without the S_{pulse} in this interval to counteract some uncertainty with regard to the timing and magnitude of this pulse, especially the likely buffering

effects of pyrite weathering on oxygenation (see details in Section 3.2, Fig. 5 and the Supplementary Information).

The time-dependent forcing function for gypsum/evaporite weathering input is modified from Shields et al. (2019) and observed $^{87}Sr/^{86}Sr$ records (Fig. 4d), and is expressed as:

$$S_{pulse} = interp1([630\ 575\ 572\ 570\ 567\ 541],\ [0\ 0\ 7\ 7\ 0\ 0]) \quad (4)$$

where the first vector is time of interpolation points (million years ago) and the second vector is the additional sulfate input, relative to today's sulfate weathering flux. For the model run in this study, steady-state 'background' and additional sulfate weathering fluxes are described as the following:

$$gypw_y = k_{gypw\_y} \cdot \left[\left(\frac{GYP_{yt}}{GYP_{y0}}\right) \cdot \left(\frac{carbw_{yt}}{k_{carbw_y}}\right) + S_{pulse}\right] \quad (5)$$

where k_{gypw_y} and k_{carbw_y} are the present-day weathering rates of young gypsum/evaporite and carbonate carbon, respectively, and $carbw_{yt}$ is the weathering rate of young carbonate. Pyrite oxidation shows a dependence on atmospheric O_2 that is reasonably approximated by the original square root dependence used in GEOCARBSULF:

$$pyrw_y = k_{pyrw\_y} \cdot \left[\left(\frac{PYR_{yt}}{PYR_{y0}}\right) \cdot \left(\frac{O}{O_0}\right)^{0.5}\right] \quad (6)$$

where k_{pyrw_y} is the present-day weathering rate of young pyrite, and O and O_0 represent the mass of atmospheric oxygen at time t and the present day, respectively. Our IMB-COPSE model assumes that part of the additional sulfate pulse was buried as gypsum, whose rate is linearly proportional to both the normalized marine sulfate and calcium concentrations; the rest is buried as pyrite to stabilize the marine sulfate reservoir. A partitioning constant f_{pyrite} = 0.2 is used to determine what fraction of pulsed sulfate input is buried as pyrite (Shields et al., 2019), which was based on what was required in their model to drive the $\delta^{13}C$ excursion form the given sulfate input, and seems broadly reasonable for an anoxic ocean:

$$mpsb_{tot} = B(PYR) + k_{gypw\_y} \cdot S_{pulse} \cdot f_{pyrite} \quad (7)$$

$$mgsb_{tot} = k_{mgsb} \cdot \left(\frac{S_t}{S_0}\right) \cdot CAL + (1 - f_{pyrite}) \cdot \left(\frac{S_t}{S_0}\right) \cdot k_{gypw\_y} \cdot S_{pulse} \cdot CAL \quad (8)$$

where k_{mgsb} and CAL are the present-day burial rates of marine gypsum/evaporite and normalized marine calcium concentrations, respectively. For completeness, we also test a scenario where there is no additional sulfate input to the oceans during the SE, and the results of this test are presented in the Supplementary Information.

297 **2.5 Initial steady-state computations**

298 The early Ediacaran atmosphere-ocean system is considered to have been depleted in pO_2 and
299 SO_4^{2-} (Lyons et al., 2014), but with high atmospheric pCO_2, potentially as a result of the prolonged
300 and severe Cryogenian Marinoan glaciation [see review by Sansjofre et al. (2011) and references
301 therein]. We chose the starting model state to have pO_2 = 0.05 PAL, $[SO_4^{2-}]_{sw}$ = 0.08 present oceanic
302 level (POL; i.e., ~2.3 mM), and pCO_2 = ~8 PAL. The 0.05 PAL pO_2 is consistent with the average of
303 recent modelling of Proterozoic O_2 regulation (0.01 ~ 0.1 PAL) and with constraints on pO_2 from the
304 absence of detrital pyrite (Daines et al., 2017). We adopt the 0.08 POL of $[SO_4^{2-}]_{sw}$ from previous
305 modelling reconstructions using geochemical proxies that proposed low $[SO_4^{2-}]_{sw}$ (~2 mM) before the
306 SE (Loyd et al., 2012; Osburn et al., 2015). High pCO_2 in the aftermath of the Marinoan glaciation
307 (~635 Ma) has been inferred from boron, triple oxygen and paired carbon isotopes [see review by
308 Sansjofre et al. (2011) and references therein]. Our initial atmospheric-oceanic dissolved inorganic
309 carbon (DIC) reservoir is set by the model steady state requirements and results at ~8 times PAL,
310 which matches the upper limit of Sansjofre et al. (2011).

311 A model steady-state with low pO_2 and low $[SO_4^{2-}]_{sw}$ in the IMB-COPSE model requires low
312 range of the C and S isotopes and thus low rates of organic carbon and pyrite burial. Thus, we chose
313 the minimum $\delta^{13}C_{carb}$ and $\delta^{34}S$ values for the three study regions at ~630 Ma as initial compositions
314 for the ocean-atmosphere C-S isotope reservoirs and sulfur isotopic fractionation (i.e., $\delta^{13}C_{carb}$ = –
315 1‰, $\delta^{34}S_{CAS}$ = 20‰ and $\Delta^{34}S$ = 8‰; Fig. 2) (see detailed discussion in the Supplementary
316 Information). We first run the IMB-COPSE model with solving steps (maximum 0.01 Myr/step) for
317 10 million years, with all the forcings and the C-S isotopic values held constant, as a spin-up to
318 achieve an initial steady state. Subsequently, the model utilizes the measured geochemical data for
319 reconstruction of Ediacaran pO_2 and $[SO_4^{2-}]_{sw}$ evolution.

320

321 **3. Results and discussion**

322 **3.1 Patterns of integrated $\delta^{13}C$ and $\delta^{34}S$ records**

323 Figure 2 shows the integrated high-resolution carbon-sulfur isotope records of the Ediacaran
324 units from Oman, South China and USA-Mexico after data screening, indicating multiple excursions
325 in both the $\delta^{13}C$ and $\delta^{34}S$ records. The screened $\delta^{13}C$ and $\delta^{34}S$ records show generally parallel negative
326 shifts during the SE (~575-567 Ma). With the similar nadir in $\delta^{13}C_{carb}$ (ca. –10 ‰) during the SE in

the each of these three regions, their $\delta^{34}S_{CAS}$ records show significant negative excursions with different magnitude (Fig. 2). The $\delta^{34}S_{CAS}$ profile exhibits a shift of –8 ‰, from ~+30 ‰ to ~+22 ‰ in Oman (Fike et al., 2006), a shift of –17 ‰, from ~+32 ‰ to ~+15 ‰ in South China (Shi et al., 2018), and a shift of –10 ‰, from ~+27 ‰ to ~+17 ‰ in USA-Mexico (Loyd et al., 2012). The generally parallel negative excursions in $\delta^{13}C_{carb}$ and $\delta^{34}S_{CAS}$ records proposed possible net sulfur inputs of isotopically lighter member (e.g., Tonian gypsum deposits, see Section 2.4) partially buffered the effects of pyrite burial on seawater $\delta^{34}S$, eventually forcing seawater sulfate to trend toward the isotopic compositions of this isotopically lighter member (Shields et al., 2019). The difference in $\delta^{34}S_{CAS}$ records has been explained as the lateral heterogeneity in $\delta^{34}S_{CAS}$ and sulfate concentration in stratified, poor-sulfate Neoproterozoic oceans (e.g., Li et al., 2010, 2020). An overall increase in $\Delta^{34}S$ across the Ediacaran Period appears in the each of these three regions (Fig. 2), indicating an increase to $[SO_4^{2-}]_{sw}$ >200 μM and unlimited expression of MSR fractionation (e.g., Fike et al., 2006; Li et al., 2010; Shi et al., 2018). Due to kinetic selection during sulfate reduction, negative $\delta^{34}S_{py}$ excursions suggest increased burial flux of pyrite framboids, which further demonstrate the increase in marine sulfate level and net pyrite burial (Fig. 2).

3.2 Decoupled Ediacaran atmospheric and oceanic oxygenation

Our modelling gives similar results when using either the Oman, South China or USA-Mexico datasets (compared to the combined C-S isotope records in Fig 5a-c), whereby all show a monotonic increase in pO_2 from ~630 Ma to ~590 Ma (i.e., atmospheric oxygenation), followed by more stable pO_2 for the rest of the Ediacaran (Fig. 5d). These results for pO_2 are generally contrary to $[SO_4^{2-}]_{sw}$ evolution (Fig. 5e). Using the Oman dataset to drive our model results in gradually rising levels of oceanic sulfate coincident with the pO_2 rise, but using the South China and USA-Mexico datasets, the model results in a general decrease in $[SO_4^{2-}]_{sw}$ to <2 mM before ~575 Ma (i.e., by the onset of the SE). However, all model runs generate a large pulsed increase in $[SO_4^{2-}]_{sw}$ in response to sulfate input over the SE from ~575 Ma (i.e., oceanic oxidation/oxygenation), which differs from the generally stable pO_2 observed over this interval.

Our model results for $[SO_4^{2-}]_{sw}$ match previous estimates of <1.2 mM in Oman (Osburn et al., 2015) and <2 mM in USA-Mexico (Loyd et al., 2012) before the SE, and up to 8 mM in South China during the SE (Shi et al., 2018) (Fig. 1d), as well as oceanic redox reconstructions based on a variety

of geochemical proxies (Fig. 1c) (e.g., Canfield et al., 2007, 2008; Hardisty et al., 2016; Sahoo et al., 2016; Zhang et al., 2019). The difference in modeled $[SO_4^{2-}]_{sw}$ trends for the early Ediacaran between Oman and South China/USA-Mexico is mainly caused by the much smaller net pyrite sulfur burial fluxes when using the Oman dataset relative to South China and USA-Mexico by 575 Ma (Fig. 5g). The large, pulsed increase in $[SO_4^{2-}]_{sw}$ after ~575 Ma is mainly driven in our model by the large pulse of evaporite weathering input during Trans-Gondwana orogenic uplift and tectonic inversion (Fig. 4b) (Shields et al., 2019). Indeed, without this additional sulfate perturbation, atmospheric O_2 levels would have significantly decreased, while the increase in $[SO_4^{2-}]_{sw}$ would have been more subdued across the SE (dotted lines in Fig. 5), due to decreased fractions of both organic carbon and pyrite burial (f_{org} and f_{py}; Fig. 5h-i). Our tests indicate that atmospheric pO_2 could potentially sustain the oxidation of the DOC pool and thus generate the Shuram $\delta^{13}C_{carb}$ anomaly (as pO_2 remains > 0) without invoking an additional evaporite sulfate pulse during this period. However, the 'no pulse' scenario is a worse fit to the previous evidence for oxygenation of deeper waters and increase in sulfate concentration that we presented in Figure 1, thus we prefer adding an additional evaporite sulfate pulse for the SE in our model.

Given the similar model results from the three regional datasets, to produce the overall estimates we take an average of the model runs, assuming that the global isotope composition of the Ediacaran oceans lies among the values recorded in Oman, USA-Mexico and South China. In this assessment (Fig. 6a-b), average pO_2 follows the patterns observed in South China and USA-Mexico, with a rise in atmospheric O_2 between ~630 and 590 Ma, followed by more stability at around 0.6 PAL for the rest of the Ediacaran, and a general decoupling with respect to $[SO_4^{2-}]_{sw}$.

Taken together, our modelling results based on independent C- and S-isotope records from three geographically-diverse continental shelves suggest that Ediacaran atmospheric oxygenation mainly occurred before ~590 Ma, whereas marine oxidation (or oxygenation) occurred mostly during the SE, indicating decoupled atmospheric and oceanic oxygenation in the Ediacaran, i.e. the atmospheric O_2 increase preceded marine oxygenation and the marine oxygenation was not related to a synchronous stepwise increase in atmospheric O_2 as we thought usually (cf. Section 1 and Figs. 6a and 6b). This finding is consistent with a previous inference that a higher Ediacaran surface-ocean organic export flux may have caused atmospheric oxygenation, but with the ocean remaining anoxic (Lenton et al., 2014). Although the absolute values of modeled pO_2 and $[SO_4^{2-}]_{sw}$ have uncertainties due to possible

387 imprecise parameters used in the model, the observation of decoupled ocean-atmosphere oxygenation
388 is particularly robust because three independent regional datasets used in the model produce this
389 behavior.
390
391 **3.3 Possible mechanism for Ediacaran atmospheric oxygenation by ~590 Ma**
392 The rise in pO_2 by 590 Ma during the early Ediacaran appears to have been driven by a major
393 net increase in organic carbon burial, coupled with a more minor increase in net pyrite sulfur burial
394 (Figs. 5f-g). These increases stem from a shift to carbon and sulfur in the surface system being fixed
395 as organic carbon and pyrite, rather than as inorganic and sulfate forms, as demonstrated by general
396 increases in the burial fraction of organic carbon over carbonate carbon (f_{org}) (Fig. 5h) and pyrite
397 sulfur over sulfate sulfur (f_{py}) (Fig. 5i) in our model. This is in accord with the deposition of basin-
398 scale organic-rich and pyrite-rich shales in the lower Doushantuo Formation, South China (e.g., Li et
399 al., 2010), coupled with scant evidence for evaporite sulfate deposition during the early Ediacaran.
400 Although our model cannot discern the driver(s) behind enhanced organic carbon burial, this may be
401 related to a rise in the dominance of eukaryotic algae (i.e., green algae) over cyanobacteria as the
402 principal marine primary producers in the aftermath of the Marinoan deglaciation (Brocks et al.,
403 2017). The rise of eukaryotic algae may have created a more efficient biological pump (BP) than the
404 previously cyanobacteria-dominated BP, thus establishing a stronger vertical organic matter export
405 to deeper oceans due to their larger nutrient storage capacity and complex behavioral strategies
406 (Lenton et al., 2014; Brocks et al., 2017).
407 This mechanism is supported by known paleotemperature records. The organic carbon
408 sequestration mentioned above would have inevitably resulted in a significant decrease in pCO_2 and
409 hence global average surface temperature prior to ~570 Ma, relative to those at the beginning of the
410 Ediacaran Period (Fig. 5j-k). Significant cooling from ~610 to ~570 Ma is consistent with the
411 Ediacaran paleotemperature reconstruction using carbonate clumped-isotope (Δ_{47}) geothermometer
412 (Chang et al., 2022), the occurrence of silicified glendonites in the middle Ediacaran Doushantuo
413 Formation, South China (Wang et al., 2017), and the occurrence of the Trinity diamictites on the
414 Bonavista Peninsula (Pu et al., 2016), which record a period of cooling temperatures leading up to
415 the non-global Gaskiers glaciation (~580 Ma). This agreement between model temperature prediction
416 and geological paleotemperature records provides additional evidence for the robustness of our

417 modeled pO_2 and $[SO_4^{2-}]_{sw}$.

418

419 **3.4 Possible mechanism for oceanic oxygenation during SE**

420 At steady state, oceanic oxygenation can be achieved when biological respiration and
421 hydrothermal reductant (e.g., Fe^{2+}) supply are overwhelmed by the ambient dissolved O_2 level, which
422 itself is controlled by oxygenic photosynthesis and the supply of O_2-rich water, following
423 downwelling at high latitudes. Taking into account the possible primary productivity levels and
424 phosphorus concentrations in the early Ediacaran oceans, atmospheric O_2 levels exceeding ~0.5-0.7
425 PAL are theoretically required to provide enough dissolved O_2 to the subsurface layer of the ocean in
426 order to maintain an oxic deep ocean (Lenton et al., 2014). Although defining such thresholds is not
427 straightforward, the early-Ediacaran long-term rise of pO_2 in our model shows that an increase in pO_2
428 to >0.6 PAL may not have overwhelmed the thresholds for deep-ocean oxygenation, but instead
429 placed the Earth system in a condition where deep ocean oxygenation could be more readily achieved.

430 Compared to the earlier deposition of banded iron formations (BIFs), the substantial appearance
431 of marine red beds at ~580 Ma has been documented to reflect a major decrease in dissolved Fe^{2+}
432 concentrations in the Ediacaran ocean (Song et al., 2017), which would be consistent with the
433 predicted Fe^{2+} oxidation and removal by the early-Ediacaran long-term rise in pO_2 we document here.
434 Furthermore, as described above, the enhanced biological pump due to the rise of green algae (see
435 Section 3.3) may have substantially lowered the total oxygen demand for organic matter degradation
436 in the early Ediacaran water column (Lenton et al., 2014). We propose that these (and potentially
437 other) processes interacting with rising pO_2 poised the Earth system close to the redox threshold for
438 widespread ocean oxygenation at ~590-575 Ma.

439 On the other hand, elevated continental weathering, as suggested by rising $^{87}Sr/^{86}Sr$ (Fig. 4d) and
440 (possible) evaporite sulfate inputs around the SE during the Trans-Gondwana orogenic uplift and
441 tectonic inversion (Fig. 4b), likely provided a trigger for transient oxygenation of the deeper ocean at
442 this time. The model results for the SE indicate that an increase in terrigenous sulfate input drove net
443 oxidation of a massive young organic carbon (e.g., DOC) reservoir (Fig. 5l), through which the
444 sulfate-derived oxidizing power was effectively transmitted into a negative $\delta^{13}C_{carb}$ signal (e.g.,
445 Rothman et al., 2003; Fike et al., 2006; McFadden et al., 2008; Li et al., 2017). Here we preferred
446 SO_4^{2-} as a direct electron acceptor of DOC oxidation due to the very large sulfate supply and lack of

447 oxygen in the deep ocean at the beginning of the SE, although oxidation via O_2 is also possible. It has
448 been suggested that this negative $\delta^{13}C_{carb}$ anomaly was driven by globally-synchronous diagenetic
449 effects (e.g., Derry, 2010), but our modeling results agree with Mg- and Ca-isotope data for SE
450 carbonates from the Wonoka Formation, Australia (Husson et al., 2015), as well as recent integrated
451 petrographic evidence (Cui et al., 2021), which support a depositional origin for the SE.
452
453 **3.5 Implications for Ediacaran metazoan diversification**
454 The decoupled oxygenation of the Ediacaran oceans and atmosphere observed in this study has
455 important implications for the rise of early animals. Ediacaran fossil records document three
456 successive assemblages, comprising the Avalon (~575-560 Ma), White Sea (~560-550 Ma) and Nama
457 (~550-540 Ma) biotas, which represent a major radiation of Ediacaran metazoans (Darroch et al.,
458 2018) (Fig. 6c). The appearance of the Ediacaran Biota has been historically linked to the
459 simultaneous [or near-synchronous] oxygenation of both the ocean and atmosphere (e.g., Sperling et
460 al., 2015b), and the rise of early animals in the Ediacaran is widely attributed to a rise in atmospheric
461 O_2 levels (e.g., Lyons et al., 2014). However, comparison of our quantitative reconstruction of
462 atmospheric and oceanic oxygenation with the Ediacaran fossil record indicates that this metazoan
463 diversification corresponds to oceanic oxygenation during the SE, rather than the gradual pre-SE
464 increase in pO_2. This highlights that a step change in oceanic oxygenation, rather than the previously
465 envisaged parallel oxygenation of the atmosphere and oceans, accompanied the radiation of early
466 animals (Zhang et al., 2019).
467
468 **4. Conclusions**
469 We compiled a large C- and S-isotope dataset from three independent paleo-continental margins
470 (Oman, South China and USA-Mexico) after strict screening for post-depositional alteration. This
471 dataset shows generally similar geochemical patterns but in different magnitude among three study
472 regions. Our isotope mass balance model, which is driven by this dataset, provides quantitative
473 support for decoupled oxygenation of the atmosphere and ocean during the Ediacaran Period. We
474 propose that atmospheric O_2 rose between ~630 Ma and ~590 Ma, setting the scene for later transient
475 ocean oxygenation, which was likely triggered by a tectonic-induced increase in continental
476 weathering and possible evaporite sulfate input; this oceanic oxygenation then created a permissive

ecological opportunity for the rise of the Ediacaran fauna. Our predicted evolution of Ediacaran atmospheric pO_2 and $[SO_4^{2-}]_{sw}$ is robust to geological background forcings and fits observed geochemical redox, paleotemperature and fossil records, providing new insight into interactions amongst global tectonics, elemental biogeochemical cycling, and early animal evolution during this critical period of Earth history. Finally, we note that this data-driven modeling work should be considered as a quantitative estimate and supplement to current proxy studies on Ediacaran atmospheric and oceanic redox evolution, which will inevitably be refined by additional proxy and modeling work in the future.

Acknowledgements

We thank Yijun Xiong, Timothy Lenton, Maoyan Zhu, Zheyu Tian, Frederick Bowyer and Junpeng Zhang for valuable discussion and constructive comments. We are also grateful to Sebastiaan van de Velde and one anonymous reviewer for their helpful comments. This study was supported by the NSFC (grants # 41825019, 42130208, 42102342, 41821001), the NSFC-RCUK_NERC program (grant # 41661134048), and the 111 project of China (grant # BP0820004). S.W.P acknowledges support from a Royal Society Wolfson Research Merit Award, and G.A.S and S.W.P acknowledge support from NERC (NE/P013643/1) through the Biosphere Evolution, Transitions and Resilience programme. A.J.K. acknowledges funding from the NERC SPHERES Doctoral Training Partnership (NE/L002574/1) and support from the ERC Consolidator grant 682760 (CONTROLPASTCO2).

CRedit authorship contribution statement

W. Shi: Data collection and analysis, Investigation, Visualization, Methodology and Writing. **B.J.W. Mills**: Supervision, Visualization, Methodology and Writing – review and editing. **C. Li**: Conceptualization, Supervision, Visualization and Writing – review and editing. **S.W. Poulton**: Supervision, Visualization, Writing – review and editing. **A.J. Krause**: Methodology and Writing – review and editing. **T. He**: Investigation, Methodology and Writing. **Y. Zhou**: Investigation, Data analysis and Writing. **M. Cheng**: Data analysis and Writing. **G.A. Shields**: Supervision, Visualization, Writing – review and editing.

Declaration of competing interest

The authors declare that they have no competing financial interests or personal relationships that could have appeared to influence the work reported in this paper.

Appendix A. Supplementary Information

Supplementary Information related to this article can be found online at xxx.

References

Ahm, A. S. C., Maloof, A. C., Macdonald, F. A., Hoffman, P. F., Bjerrum, C. J., Bold, U., Rose, C. V., Strauss, J. V., Higgins, J. A., 2019, An early diagenetic deglacial origin for basal Ediacaran "cap dolostones". Earth Planet. Sci. Lett. 506, 292-307. https://doi.org/10.1016/j.epsl.2018.10.046.

Blättler, C. L., Bergmann, K. D., Kah, L. C., Gómez-Pérez, I., Higgins, J. A., 2020, Constraints on Meso- to Neoproterozoic seawater from ancient evaporite deposits. Earth Planet. Sci. Lett. 532, 1-10. https://doi.org/10.1016/j.epsl.2019.115951.

Brennan, S. T., Lowenstein, T. K., Horita, J., 2004, Seawater chemistry and the advent of biocalcification. Geology 32, 473-476. https://doi.org/10.1130/G20251.1.

Brocks, J. J., Jarrett, A. J., Sirantoine, E., Hallmann, C., Hoshino, Y., Liyanage, T., 2017, The rise of algae in Cryogenian oceans and the emergence of animals. Nature 548, 578-581. https://doi.org/10.1038/nature23457.

Canfield, D. E., Poulton, S. W., Narbonne, G. M., 2007, Late-Neoproterozoic deep-ocean oxygenation and the rise of animal life. Science 315, 92-95. https://doi.org/10.1126/science.1135013.

Canfield, D. E., Poulton, S. W., Knoll, A. H., Narbonne, G. M., Ross, G., Goldberg, T., Strauss, H., 2008, Ferruginous conditions dominated later Neoproterozoic deep-water chemistry. Science 321, 949-952. DOI: 10.1126/science.1154499

Chang, B., Li, C., Algeo, T. J., Lyons, T. W., Shi, W., Cheng, M., Luo, G., She, Z., Xie, S., Tong, J., Zhu, M., Huang, J., Foster, I., Tripati, A., 2022, A ~60-Ma-long, high-resolution record of Ediacaran paleotemperature. Sci. Bull. 67, 910-913. https://doi.org/10.1016/j.scib.2022.01.025.

Cui, H., Kitajima, K., Orland, I. J., Xiao, S., Baele, J. M., Kaufman, A. J., Denny, A., Zhou, C., Spicuzza, M. J., Fournelle, J. H., Valley, J. W., 2021, Deposition or diagenesis? Probing the Ediacaran Shuram excursion in South China by SIMS. Global Planet. Change 206, 103591. https://doi.org/10.1016/j.gloplacha.2021.103591

Daines, S. J., Mills, B. J. W., Lenton, T. M., 2017, Atmospheric oxygen regulation at low Proterozoic levels by incomplete oxidative weathering of sedimentary organic carbon. Nat. Commun. 8, 1-11. https://doi.org/10.1038/ncomms14379.

Darroch, S. A. F., Smith, E. F., Laflamme, M., Erwin, D. H., 2018, Ediacaran extinction and Cambrian explosion. Trends Ecol. Evol. 33, 653-663. https://doi.org/10.1016/j.tree.2018.06.003.

Derry, L. A., 2010, A burial diagenesis origin for the Ediacaran Shuram-Wonoka carbon isotope anomaly. Earth Planet. Sci. Lett. 294, 152-162. https://doi.org/10.1016/j.epsl.2010.03.022.

Evans, D. A. D., 2006, Proterozoic low orbital obliquity and axial-dipolar geomagnetic field from evaporite palaeolatitudes. Nature 444, 51-55. https://doi.org/10.1038/nature05203.

Fike, D. A., Grotzinger, J. P., Pratt, L. M., Summons, R. E., 2006, Oxidation of the Ediacaran ocean.

548 Nature 444, 744-747. https://doi.org/10.1038/nature05345.
549 Grotzinger, J. P., Fike, D. A., Fischer, W. W., 2011, Enigmatic origin of the largest-known carbon
550 isotope excursion in Earth's history. Nat. Geosci. 4, 285-292. https://doi.org/10.1038/ngeo1138.
551 Hardisty, D. S., Lu, Z., Bekker, A., Diamond, C. W., Gill, B. C., Jiang, G., Kah, L. C., Knoll, A. H.,
552 Loyd, S. J. Osburn, M. R., Planavsky, N. J., Wang, C., Zhou, X., Lyons, T. W. 2017, Perspectives
553 on Proterozoic surface ocean redox from iodine contents in ancient and recent carbonate. Earth
554 Planet. Sci. Lett., 463, 159-170. https://doi.org/10.1016/j.epsl.2017.01.032.
555 Hay, W. W., Migdisov, A., Balukhovsky, A. N., Wold, C. N., Flögel, S., Söding, E., 2006, Evaporites
556 and the salinity of the ocean during the Phanerozoic: Implications for climate, ocean circulation
557 and life. Palaeogeogr. Palaeoclimatol. Palaeoecol. 240, 3-46.
558 https://doi.org/10.1016/j.palaeo.2006.03.044.
559 Husson, J. M., Higgins, J. A., Maloof, A. C., Schoene, B., 2015, Ca and Mg isotope constraints on
560 the origin of Earth's deepest $\delta^{13}C$ excursion. Geochim. Cosmochim. Acta 160, 243-266.
561 https://doi.org/10.1016/j.gca.2015.03.012.
562 Kaufman, A. J., Knoll, A. H., 1995, Neoproterozoic variations in the C-isotopic composition of
563 seawater: Stratigraphic and biogeochemical implications. Precambrian Res. 73, 27-49.
564 https://doi.org/10.1016/0301-9268(94)00070-8.
565 Lenton, T. M., Boyle, R. A., Poulton, S. W., Shields, G. A., Butterfield, N. J., 2014, Co-evolution of
566 eukaryotes and ocean oxygenation in the Neoproterozoic era. Nat. Geosci. 7, 257-265.
567 https://doi.org/10.1038/ngeo2108
568 Lenton, T. M., Daines, S. J., Mills, B. J. W., 2018, COPSE reloaded: An improved model of
569 biogeochemical cycling over Phanerozoic time. Earth Sci. Rev. 178, 1-28.
570 https://doi.org/10.1016/j.earscirev.2017.12.004.
571 Li, C., Love, G. D., Lyons, T. W., Fike, D. A., Sessions, A. L., Chu, X., 2010, A stratified redox model
572 for the Ediacaran ocean. Science 328, 80-83. https://doi.org/10.1126/science.1182369
573 Li, C., Hardisty, D. S., Luo, G., Huang, J., Algeo, T. J., Cheng, M., Shi, W., An, Z., Tong, J., Xie, S.,
574 Jiao, N., Lyons, T. W., 2017, Uncovering the spatial heterogeneity of Ediacaran carbon cycling.
575 Geobiology 15, 211-224. https://doi.org/10.1111/gbi.12222.
576 Li, C., Cheng, M., Zhu, M., Lyons, T. W., 2018, Heterogeneous and dynamic marine shelf
577 oxygenation and coupled early animal evolution. Emerg. Top. Life Sci. 2, 279-288.
578 https://doi.org/10.1042/ETLS20170157.
579 Li, C., Shi, W., Cheng, M., Jin, C., Algeo, T. J., 2020, The redox structure of Ediacaran and early
580 Cambrian oceans and its controls. Sci. Bull. 65, 2141-2149.
581 https://doi.org/10.1016/j.scib.2020.09.023.
582 Loyd, S. J., Marenco, P. J., Hagadorn, J. W., Lyons, T. W., Kaufman, A. J., Sour-Tovar, F., Corsetti,
583 F. A., 2012, Sustained low marine sulfate concentrations from the Neoproterozoic to the
584 Cambrian: Insights from carbonates of northwestern Mexico and eastern California. Earth Planet.
585 Sci. Lett. 339-340, 79-94. https://doi.org/10.1016/j.epsl.2012.05.032.
586 Lu, M., Zhu, M., Zhang, J., Shields-Zhou, G., Li, G., Zhao, F., Zhao, X., Zhao, M., 2013, The
587 DOUNCE event at the top of the Ediacaran Doushantuo Formation, South China: Broad
588 stratigraphic occurrence and non-diagenetic origin. Precambrian Res. 225, 86-109.
589 https://doi.org/10.1016/j.precamres.2011.10.018.

590 Lyons, T. W., Reinhard, C. T., Planavsky, N. J., 2014, The rise of oxygen in Earth's early ocean and
591 atmosphere. Nature 506, 307-315. https://doi.org/10.1038/nature13068.
592 McFadden, K. A., Huang, J., Chu, X., Jiang, G., Kaufman, A. J., Zhou, C., Yuan, X., Xiao, S., 2008,
593 Pulsed oxidation and biological evolution in the Ediacaran Doushantuo Formation. Proc. Natl.
594 Acad. Sci. U.S.A. 105, 3197-3202. https://doi.org/10.1073/pnas.0708336105.
595 Mills, B. J. W., Belcher, C. M., Lenton, T. M., Newton, R. J., 2016, A modeling case for high
596 atmospheric oxygen concentrations during the Mesozoic and Cenozoic. Geology 44, 1023-1026.
597 https://doi.org/10.1130/G38231.1.
598 Mills, B. J. W., Scotese, C. R., Walding, N. G., Shields, G. A., Lenton, T. M., 2017, Elevated CO_2
599 degassing rates prevented the return of Snowball Earth during the Phanerozoic. Nat. Commun.
600 8, 1-7. https://doi.org/10.1038/s41467-017-01456-w.
601 Och, L. M. and Shields-Zhou, G. A., 2012, The Neoproterozoic oxygenation event: Environmental
602 perturbations and biogeochemical cycling. Earth-Sci. Rev. 110, 26-57.
603 https://doi.org/10.1016/j.earscirev.2011.09.004.
604 Osburn, M. R., Owens, J., Bergmann, K. D., Lyons, T. W., Grotzinger, J. P., 2015, Dynamic changes
605 in sulfate sulfur isotopes preceding the Ediacaran Shuram Excursion. Geochim. Cosmochim.
606 Acta 170, 204-224. https://doi.org/10.1016/j.gca.2015.07.039.
607 Pogge Von Strandmann, P. A. E., Stüeken, E. E., Elliott, T., Poulton, S. W., Dehler, C. M., Canfield,
608 D. E., Catling, D. C., 2015, Selenium isotope evidence for progressive oxidation of the
609 Neoproterozoic biosphere. Nat. Commun. 6, 1-10. https://doi.org/10.1038/ncomms10157.
610 Poulton, S. W., Bekker, A., Cumming, V. M., Zerkle, A. L., Canfield, D. E., Johnston, D. T., 2021, A
611 200-million-year delay in permanent atmospheric oxygenation. Nature 592, 232-236.
612 https://doi.org/10.1038/s41586-021-03393-7.
613 Pu, J. P., Bowring, S. A., Ramezani, J., Myrow, P., Raub, T. D., Landing, E., Mills, A., Hodgin, E.,
614 Macdonald, F. A., 2016, Dodging snowballs: Geochronology of the Gaskiers glaciation and the
615 first appearance of the Ediacaran biota. Geology 44, 955-958. https://doi.org/10.1130/G38284.1
616 Rooney, A. D., Cantine, M. D., Bergmann, K. D., Gómez-Pérez, I., Al Baloushi, B., Boag, T. H.,
617 Busch, J. F., Sperling, E. A., Strauss, J. V., 2020, Calibrating the coevolution of Ediacaran life
618 and environment. Proc. Natl. Acad. Sci. U.S.A. 117, 16824-16830.
619 https://doi.org/10.1073/pnas.2002918117
620 Rothman, D. H., Hayes, J. M., Summons, R. E., 2003, Dynamics of the Neoproterozoic carbon cycle.
621 Proc. Natl. Acad. Sci. U.S.A. 100, 8124-8129. https://doi.org/10.1073/pnas.0832439100.
622 Sahoo, S. K., Planavsky, N. J., Jiang, G., Kendall, B., Owens, J. D., Wang, X., Shi, X., Anbar, A.D.,
623 Lyons, T. W., 2016, Oceanic oxygenation events in the anoxic Ediacaran
624 ocean. Geobiology 14(5), 457-468. https://doi.org/10.1111/gbi.12182.
625 Sansjofre, P., Ader, M., Trindade, R. I. F., Elie, M., Lyons, J., Cartigny, P., Nogueira, A. C. R., 2011,
626 A carbon isotope challenge to the snowball Earth. Nature 478, 93-96.
627 https://doi.org/10.1038/nature10499
628 Sawaki, Y., Ohno, T., Tahata, M., Komiya, T., Hirata, T., Maruyama, S., Windley, B. F., Han, J., Shu,
629 D., Li, Y., 2010, The Ediacaran radiogenic Sr isotope excursion in the Doushantuo Formation in
630 the Three Gorges area, South China. Precambrian Res. 176, 46-64.
631 https://doi.org/10.1016/j.precamres.2009.10.006.
632 Shi, W., Li, C., Luo, G., Huang, J., Algeo, T. J., Jin, C., Zhang, Z., Cheng, M., 2018, Sulfur isotope

633 evidence for transient marine-shelf oxidation during the Ediacaran Shuram Excursion. Geology
634 46, 267-270. https://doi.org/10.1130/G39663.1
635 Shields, G. A., Mills, B. J. W., Zhu, M., Raub, T. D., Daines, S. J., Lenton, T. M., 2019, Unique
636 Neoproterozoic carbon isotope excursions sustained by coupled evaporite dissolution and pyrite
637 burial. Nat. Geosci. 12, 823-827. https://doi.org/10.1038/s41561-019-0434-3.
638 Song, H., Jiang, G., Poulton, S. W., Wignall, P. B., Tong, J., Song, H., An, Z., Chu, D., Tian, L., She,
639 Z., Wang, C., 2017, The onset of widespread marine red beds and the evolution of ferruginous
640 oceans. Nat. Commun. 8, 1-7. https://doi.org/10.1038/s41467-017-00502-x.
641 Sperling, E. A., Wolock, C. J., Morgan, A. S., Gill, B. C., Kunzmann, M., Halverson, G. P.,
642 Macdonald, F. A., Knoll, A. H., Johnston, D. T., 2015a, Statistical analysis of iron
643 geochemical data suggests limited late Proterozoic oxygenation. Nature 523, 451-454.
644 https://doi.org/10.1038/nature14589.
645 Sperling, E. A., Knoll, A. H., Girguis, P. R., 2015b, The ecological physiology of Earth's second
646 oxygen revolution. Annu. Rev. Ecol. Evol. Syst. 46, 215-235. https://doi.org/10.1146/annurev-
647 ecolsys-110512-135808.
648 Tostevin, R., He, T., Turchyn, A. V., Wood, R. A., Penny, A. M., Bowyer, F., Antler, G., Shields, G.
649 A., 2017, Constraints on the late Ediacaran sulfur cycle from carbonate associated sulfate.
650 Precambrian Res. 290, 113-125. https://doi.org/10.1016/j.precamres.2017.01.004.
651 Voice, P. J., Kowalewski, M., Eriksson, K. A., 2011, Quantifying the timing and rate of crustal
652 evolution: Global compilation of radiometrically dated detrital zircon grains. J. Geol. 119, 109-
653 126. https://doi.org/10.1086/658295.
654 Wang, Z., Wang, J., Suess, E., Wang, G., Chen, C., Xiao, S., 2017, Silicified glendonites in the
655 Ediacaran Doushantuo Formation (South China) and their potential paleoclimatic
656 implications. Geology 45, 115-118. https://doi.org/10.1130/G38613.1.
657 Wei, G., Ling, H., Shields, G. A., Chen, T., Lechte, M., Chen, X., Chen, Q., Lei, H., Zhu, M., 2019,
658 Long-term evolution of terrestrial inputs from the Ediacaran to early Cambrian: Clues from Nd
659 isotopes in shallow-marine carbonates, South China. Palaeogeogr. Palaeoclimatol. Palaeoecol.
660 535, 109367. https://doi.org/10.1016/j.palaeo.2019.109367.
661 Williams, J. J., Mills, B. J. W., Lenton, T. M., 2019, A tectonically driven Ediacaran oxygenation
662 event. Nat. Commun. 10, 1-10. https://doi.org/10.1038/s41467-019-10286-x.
663 Xiao, S., Narbonne, G. M., Zhou, C., Laflamme, M., Grazhdankin, D. V., Moczydłowska-Vidal, M.,
664 Cui, H., 2016, Towards an Ediacaran time scale: Problems, protocols, and prospects. Episodes
665 39, 540-555. https://doi.org/10.18814/epiiugs/2016/v39i4/103886.
666 Yang, C., Rooney, A. D., Condon, D. J., Li, X., Grazhdankin, D. V., Bowyer, F. T., Hu, C., McCdonald,
667 F. A., Zhu, M., 2021, The tempo of Ediacaran evolution. Sci. adv. 7(45), 1-10. DOI:
668 10.1126/sciadv.abi9643
669 Zhang, F., Xiao, S., Romaniello, S. J., Hardisty, D., Li, C., Melezhik, V., Pokrovsky, B., Cheng, M.,
670 Shi, W., Lenton, T. M., Anbar, A. D., 2019, Global marine redox changes drove the rise and fall
671 of the Ediacara biota. Geobiology 17, 594-610. https://doi.org/10.1111/gbi.12359.
672

673 **Figures and captions**

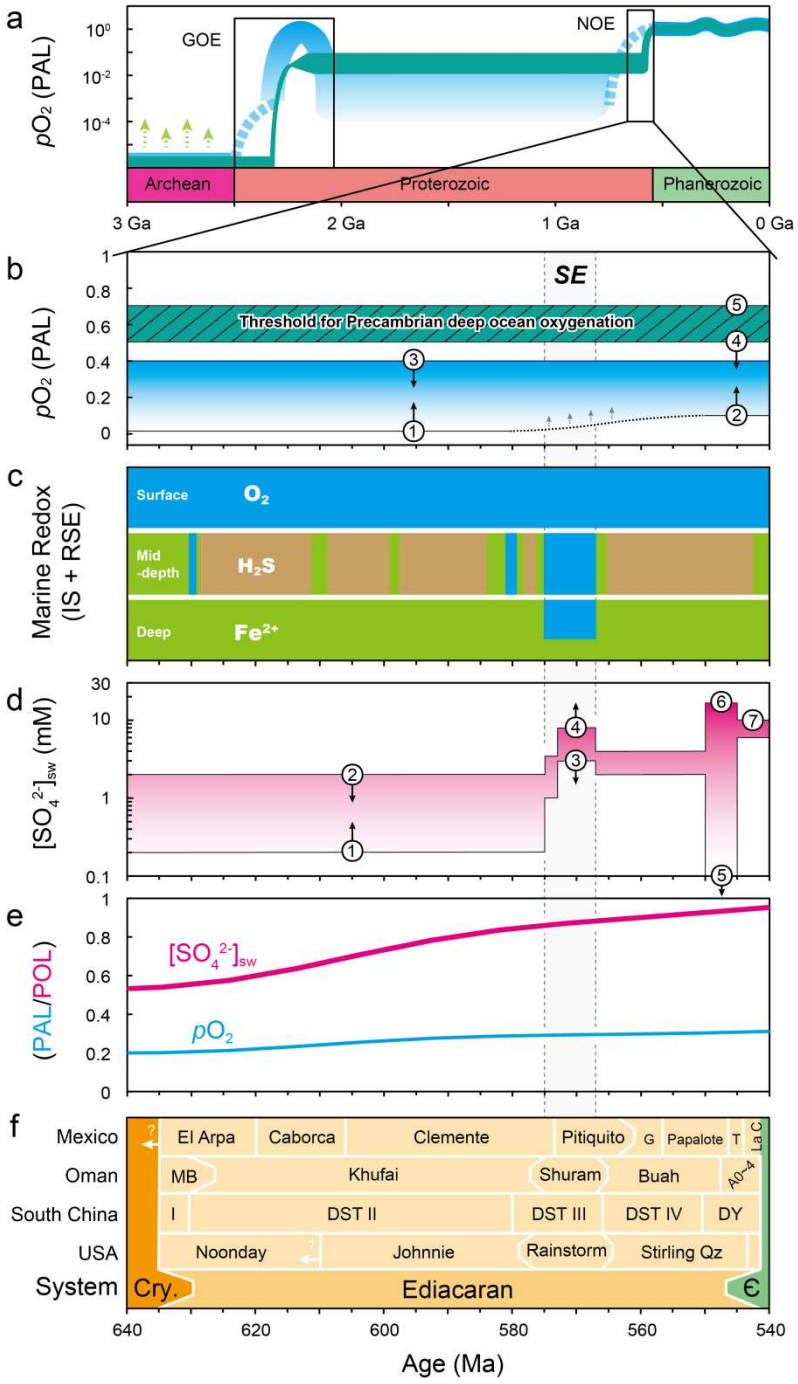

674

675 **Fig. 1. Earth's redox history with a focus on the Ediacaran Period. a.** Atmospheric O_2 evolution (Lyons et
676 al., 2014). **b.** Previous estimations of Ediacaran atmospheric O_2 levels based on redox sensitive trace-metal
677 inventories, biological physiological thresholds and a simple three-box ocean model. pO_2 constraints include:
678 ① a minimum O_2 level of 0.005~0.01 present atmospheric level (PAL), required for the disappearance of mass-
679 dependent sulfur isotope fractionation, red beds, and the earliest animals; ② O_2 levels exceeding 0.1 PAL
680 required to explain the lack of detrital pyrite in the Proterozoic (Daines et al., 2017), and pO_2 requirements by
681 Cambrian biota (Sperling et al., 2015b); ③ and ④ an upper pO_2 limit of less than ~0.4-0.5 PAL for the
682 presence of persistently anoxic deep waters with modern day oceanic phosphorus concentrations; and ⑤ an

upper pO_2 limit of 0.7 PAL to maintain Precambrian deep-oceanic anoxia, when a positive feedback between bottom-water anoxia and phosphorus recycling from sediments is taken into consideration (see review by Lenton et al., 2014). **c.** A summary of Ediacaran marine redox reconstruction by iron speciation (IS) and redox sensitive element (RSE) proxies (Canfield et al., 2007, 2008; Hardisty et al., 2017; Li et al., 2018; Sahoo et al., 2016; Zhang et al., 2019). **d.** A summary of Ediacaran marine sulfate concentration reconstructions: ① sulfate levels exceeding ~200 μM required to achieve full S-isotopic fractionation during microbial sulfate reduction (MSR) (Fike et al., 2006); ② a maximum sulfate concentration of <2 mM before the Shuram carbonate C-isotope Excursion (SE) event (Loyd et al., 2012; Osburn et al., 2015); ③ and ④, an increase in marine sulfate concentration and a possible lateral sulfate gradient from proximal (>8 mM) to distal (<3 mM) during the SE event (Shi et al., 2018); ⑤ a maximum sulfate concentration of <30 μM for the occurrence of super-heavy pyrite isotopes, as found in Namibia (e.g., Tostevin et al., 2017); ⑥ a sulfate maximum of ~17 mM as inferred from multiple sulfur isotope and fluid inclusion data (e.g., Brennan et al., 2004); ⑦ an estimated sulfate reconstruction of 6-10 mM from calcium isotopes in evaporite deposits (Blättler et al., 2018). **e.** Previous estimation of atmospheric O_2 (blue line) and marine sulfate (magenta line) levels using the standard COPSE model (Williams et al., 2019). **f.** Stratigraphic sequences and chronological framework for the study regions (e.g., Fike et al., 2006; McFadden et al., 2008; Loyd et al., 2012) (given as formations, except members [I-IV], the age model is taken from Rooney et al. [2020]). Abbreviations: SE = Shuram Excursion; GOE = Great Oxidation Event; NOE = Neoproterozoic Oxygenation Event; G = Gamuza, T = Tecolote, La C = La Cienega, DST (I-IV) = Doushantuo Formation (Member I-IV), DY = Dengying Formation, MB = Masirah Bay Formation, A0~4 = Ara unit 0 to 4, Cry. = Cryogenian, Є = Cambrian.

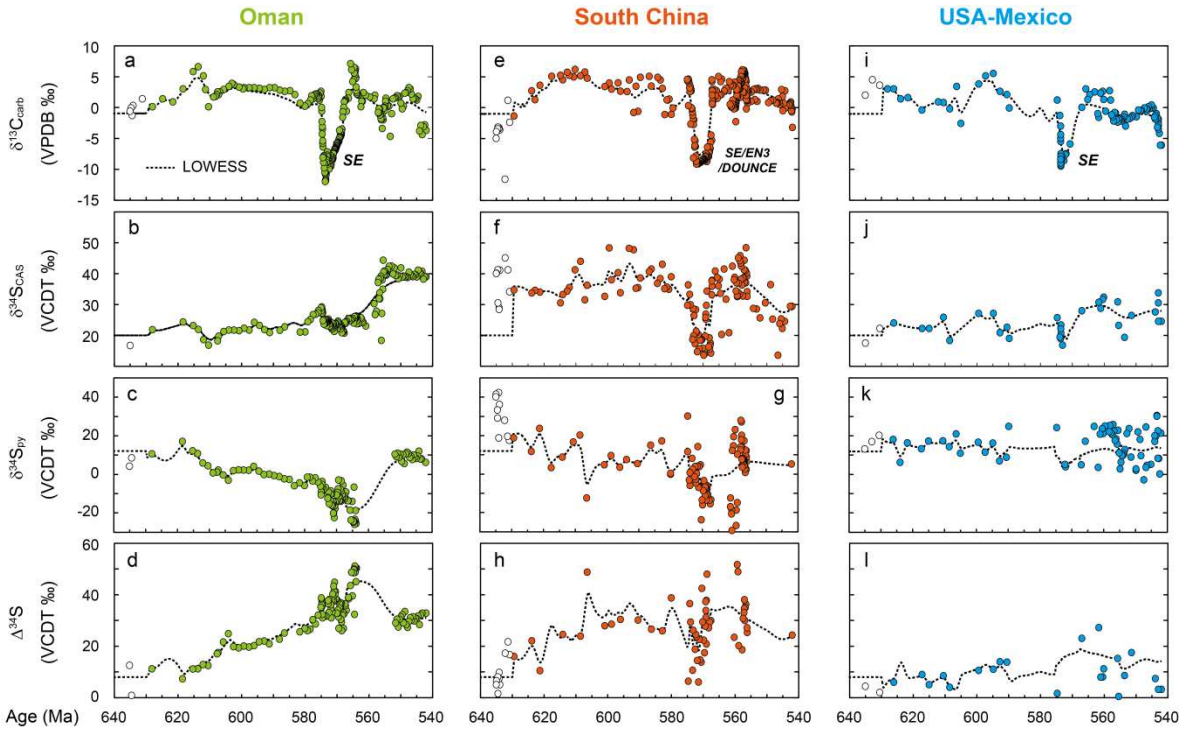

Fig. 2. Integrated Ediacaran C-S isotope records from three study regions (Oman, South China and USA-Mexico). Note that samples for the 635-630 Ma period (i.e., unfilled circles) are not used in the model runs

because these samples are considered to have been deposited in the Ediacaran cap-carbonate non-steady state, see main text for details. Abbreviations: SE = Shuram Excursion; EN3 = Ediacaran negative excursion 3; DOUNCE = Doushantuo negative $\delta^{13}C_{carb}$ excursion; VPDB = Vienna Pee Dee Belemnite; VCDT = Vienna Canyon Diablo Troilite; LOWESS = LOcally WEighted Scatterplot Smoothing. The raw data and their sources are given in Table S8.

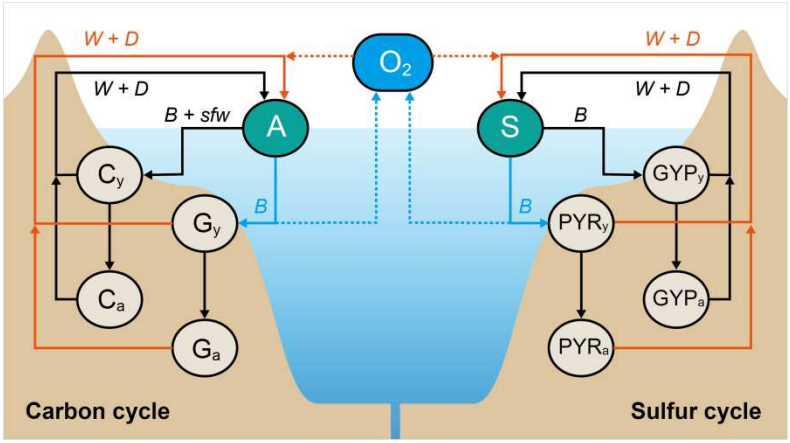

Fig. 3. Long-term C-S-O cycles in the IMB-COPSE model. Atmospheric-oceanic carbon (A) and sulfate (S) are removed into crustal reservoirs (G, organic carbon; C, carbonate; PYR, pyrite; GYP, gypsum) through burial (B) and sea-shelf weathering (sfw) fluxes, but are returned by weathering (W) and degassing (D). Atmospheric oxygen is sourced by the burial of organic carbon and pyrite, but removed by weathering and degassing of the same species. Subscript "y" and "a" denote young and ancient crustal reservoirs, respectively. Modified from Mills et al. (2016).

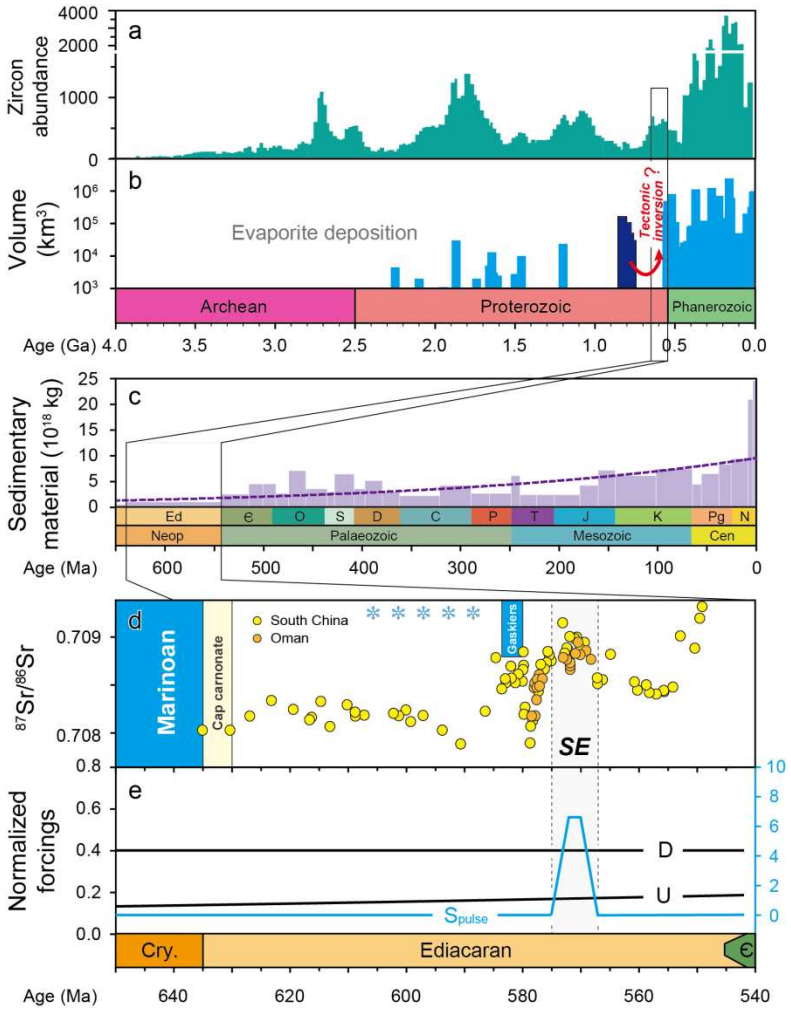

721

722 **Fig. 4. Major background geological forcings involved in our IMB-COPSE modeling for the Ediacaran.**
723 **a.** A compilation of zircon abundance (Voice et al., 2011). **b.** Evaporite basin depositional records through Earth
724 history (Evans, 2006). The dark blue shade represents evaporite deposits of Tonian age, which may have been
725 exposed with tectonic inversion relating to the formation of Gondwanaland (c.f., Shields et al., 2019). **C.**
726 Existing masses of sediment on global continent blocks and in the global ocean basins (shaded area), and an
727 exponential decay curve fit through the data (dashed line) (Hay et al., 2006). **D.** Strontium isotope records
728 ($^{87}Sr/^{86}Sr$) for carbonates from South China and Oman during the Ediacaran (Sawaki et al., 2010 and see review
729 by Li et al., 2017). **E.** Assumed major forcings of uplift (U), degassing (D), and an additional sulfate pulse
730 (S_{pulse}) of sulfate weathering during the Ediacaran.
731

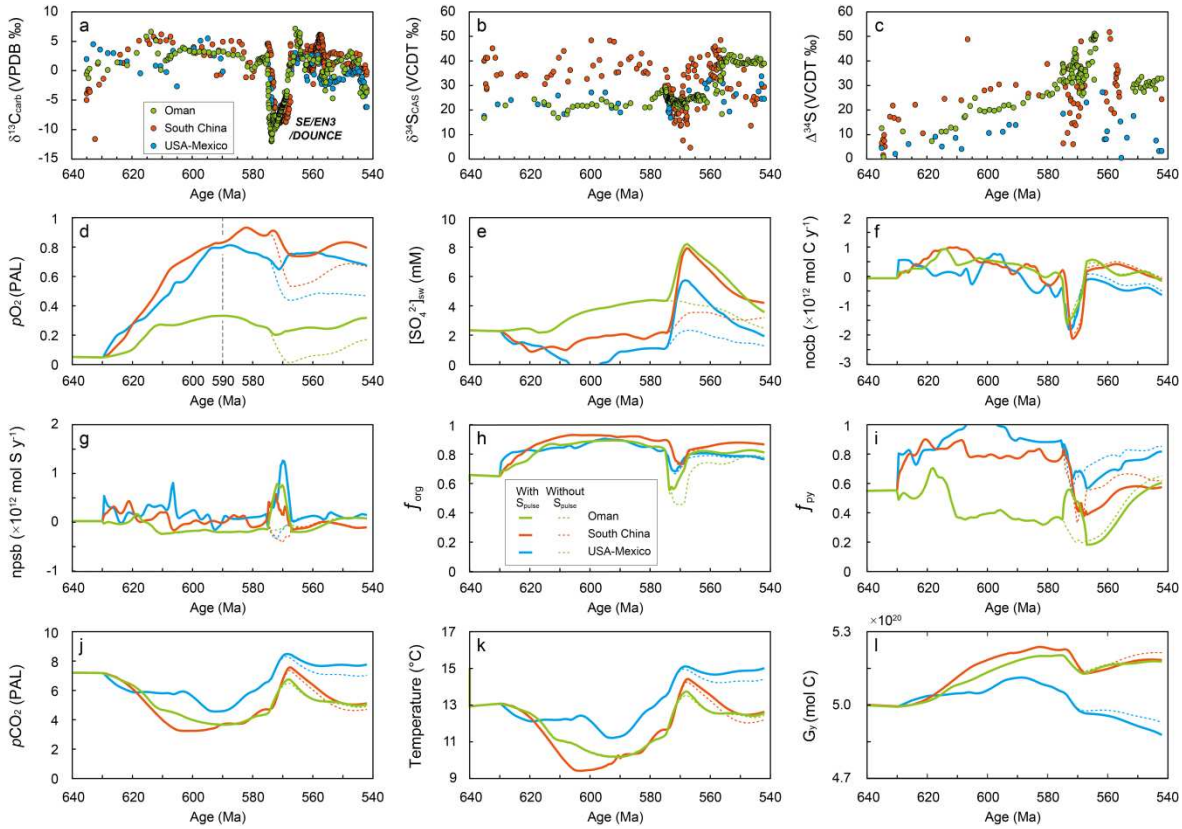

Fig. 5. Combined C-S isotopic records and the IMB-COPSE model outputs in this study with (full lines) versus without (dotted lines) the additional evaporite (gypsum) weathering inputs during the Shuram Excursion (SE). a. Combined $\delta^{13}C_{carb}$ records. **b.** Combined $\delta^{34}S_{CAS}$ records. **c.** Combined $\Delta^{34}S$ records. **d.** Atmospheric O_2 level (pO_2). **e.** Oceanic sulfate concentration ($[SO_4]_{sw}$). **f.** Flux of net organic carbon burial (nocb). **g.** Flux of net pyrite sulfur burial (npsb). **h.** Burial fraction of organic carbon (f_{org}). **i.** Burial fraction of pyrite sulfur (f_{py}). **j**. Atmospheric CO_2 level (pCO_2). **k.** Global average temperature. **l.** Mass of the young organic carbon reservoir (G_y). PAL = present atmospheric level.

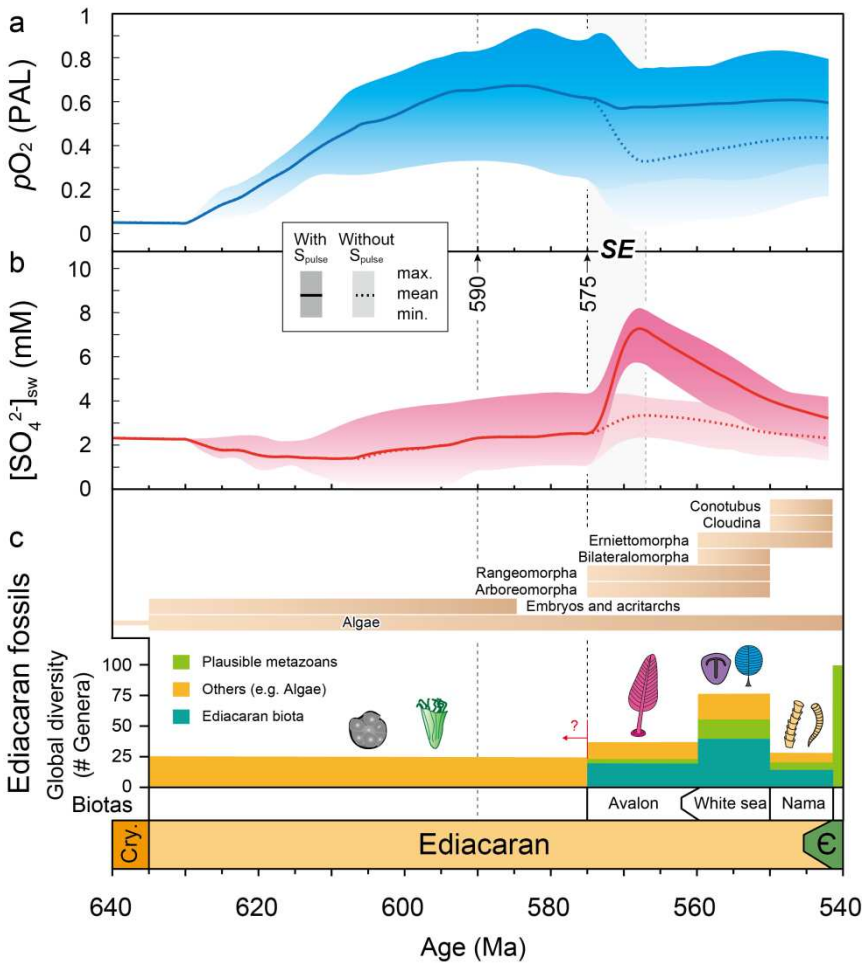

741

742 **Fig. 6. Summary of the key outputs from the IMB-COPSE model and their comparison with coeval fossil**
743 **records. A.** Ediacaran atmospheric pO_2. **B.** Ediacaran seawater sulfate concentration ($[SO_4^{2-}]_{sw}$). **c.** A
744 compilation of Ediacaran fossils (Darroch et al., 2018; Rooney et al., 2020). The "max.", "mean", and "min."
745 in (**a**) and (**b**) are the maximum, mean, and minimum of modelled atmospheric pO_2 and $[SO_4^{2-}]_{sw}$, respectively.
746 See text for details.